Supplementary Information (SI) for Chemical Science.

Active Selenium-Driven Confined Crystallization and Carrier Dynamics in High-Efficiency Ultrathin Semi-Transparent Sb_2Se_3 Solar Cells

Huafei Guo [a,c,*], Bangzhi Shen [a], Xing Wang [d], Jiayu Xiao [a], Wenyun Deng [a], Sai Jiang [a], Lei Xu [d], Xu Dong [c,*], Lvzhou Li [c], Shuai Zhang [b], Jianhua Qiu [a,*], Ningyi Yuan [b], and Jianning Ding [c]

[a]Wang Zheng School of Microelectronics, Changzhou University, Changzhou 213164, China.
E-mail: guohuafei@cczu.edu.cn; jhqiu@cczu.edu.cn
[b]School of Materials Science and Engineering, Changzhou University, Changzhou 213164, China.
E-mail: guohuafei@cczu.edu.cn
[c]Institute of Technology for Carbon Neutralization, School of Physical Science and Technology, Yangzhou University, Yangzhou 225127, China.
E-mail: guohuafei@cczu.edu.cn, xudong@yzu.edu.cn
[d]School of Flexible Electronics (Future Technologies), Institute of Advanced Materials (IAM), Nanjing Tech University, Nanjing 211816, China.

Table S1. Fitting parameters of the bi-exponential decay model for the TAS kinetics of W/O KOH and W KOH samples.

Sample	**A1**	**τ1(ps)**	**A2**	**τ2(ps)**
W/O KOH	0.3087	45.67	0.3741	1311.54
W KOH	0.2288	67.43	0.3099	1878.35

Table S2. Fitting parameters of the bi-exponential decay model for the TPV transients of W/O Se and W Se devices.

Sample	**A1**	**τ1(μs)**	**A2**	**τ2(μs)**
W/O Se	0.8122	12.139	0.1034	84.474
W Se	0.3560	15.394	0.5347	76.783

Table S3. Fitting parameters of the bi-exponential decay model for the TPC transients of W/O Se and W Se devices.

Sample	**A1**	**τ1(μs)**	**A2**	**τ2(μs)**
W/O Se	0.6101	0.2642	0.3991	0.205
W Se	0.4298	0.162	0.5714	0.226

Table S4. Fitting parameters of the bi-exponential decay model for the TAS kinetics of W/O Se and W Se samples.

Sample	**A1**	**τ1(ps)**	**A2**	**τ2(ps)**
W/O Se	0.4099	59.60	0.5999	4.821
W Se	0.4066	137.88	0.5935	12.967

Note 1: Detailed process of experimental and theoretical calculations

Preparation of CdS film

First, FTO (F-doped Tin Oxide) glass (from Libo New Energy Technology Co., Ltd., Yingkou, China) was cleaned in an ultrasonic cleaner for 30 minutes each with detergent, deionized water, acetone, and ethanol. The washed FTO glass was nitrogen-dried and treated with ozone plasma for 20 minutes. The CdS film was then formed using the chemical bath deposition (CBD) method. The FTO glass was placed in a beaker, followed by the sequential addition of 20 mL of cadmium sulfate ($CdSO_4$) solution (0.015 mol/L), 20 mL of thiourea (CH_4N_2S) solution (0.75 mol/L), 20 mL of ammonia solution ($NH_3 \cdot H_2O$, 25%-28%), 1 mL of potassium hydroxide (KOH) solution (5 mol/L), and 140 mL of deionized water. The mixture was continuously stirred at 60 °C for 15 minutes. Following the reaction, the substrates were removed, rinsed with deionized water, and dried with nitrogen. A cadmium chloride-methanol ($CdCl_2$-CH_3OH, 0.2 mg/mL) solution was then used post-treatment, followed by 5 minutes of annealing in air at 400 °C.

Preparation of Sb_2Se_3 film and device

During the preparation of Sb_2Se_3 thin films on CdS electron transport layers, the pre-dried Sb_2Se_3 powder (0.7 g) was initially spread uniformly on a glass slide. This slide was then positioned on an aluminum nitride (AIN) ceramic plate within a rapid thermal annealing furnace, with the CdS-coated glass substrate facing the Sb_2Se_3 powder while maintaining a 10 mm separation. Graphite blocks were employed to cover the assembly for temperature stabilization. The chamber was evacuated to 2.0×10^{-3} Torr before heating the sample to 300°C with a 1200 second dwell time, followed by rapid ramping to 580°C for 60-second maintenance, enabling Sb_2Se_3 film growth on the CdS surface to form an approximately 50 nm thick absorber layer. Following Sb_2Se_3 film formation, a Se capping layer was deposited via magnetron sputtering. The sample was secured on a rotating stage inside a vacuum chamber, aligned parallel to the Se target at 10 cm separation. After evacuating to 2×10^{-4} Torr, the substrate was heated to 200°C under 0.005 Torr working pressure. Sputtering was conducted using 99.99% purity Se target with 22 W radio frequency power for 60 seconds, yielding a 10 nm thick Se layer. Substrate rotation at 15 revolutions per minute ensured film uniformity. The sample was retrieved after natural cooling to ambient temperature.

Characterization

The crystalline planar structure and arrangement of the corresponding Sb_2Se_3 film were determined using XRD analysis on a Smart Apex II DUO (Bruker-AXS). The films' molecular structure and surface defects were investigated with a Thermo Fisher DXR2 Raman spectrometer. The chemical states, elemental migration, and energy states of Sb_2Se_3 films were studied using X-ray photoelectron spectroscopy (XPS, Thermo Scientific K-Alpha) and ultraviolet photoelectron spectroscopy (UPS) on a PHI 5000 VersaProbe III. The surface and cross-sectional SEM topography of the corresponding Sb_2Se_3 film were measured using a FESEM NOVA NANOSEM 4800. The solar cells' external quantum efficiency (EQE) was measured using a QEXL photovoltaic characterization system from PV Measurements. The overall output efficiency was measured with an I-V tester under AM 1.5G illumination at 1000 W/m^2. A Keysight E4980AL Precision LCR meter, with a DC bias voltage range of -1 to 2 V, was used to measure capacitance-voltage (C-V) and drive-level capacitance profiling (DLCP) at 25 °C and 10 kHz in total darkness. Electrochemical impedance spectroscopy (EIS) was carried out in the dark between 1 Hz and 4 MHz using a bias voltage of -0.6 V. The devices' transient photovoltage and photocurrent were measured using a TranPVC S900 nanosecond pulsed laser with a wavelength of 517 nm, pulse width of 18 ns, and laser line width of 4 nm. The carrier lifetime of the corresponding CdS films was estimated using transient absorption spectroscopy (TAS) results obtained with a pump-probe system (Helios, Ultrafast Systems). The carrier lifetime of the corresponding Sb_2Se_3 film was fitted using TAS data collected with Coherent's Ti: sapphire laser system (800 nm, 35 fs, 6 mJ/pulse, and 1kHz repetition rate) and the TOPAS Optical Parametric Amplifier (OPA). A Phystech FT-1230 HERA DLTS device was used to obtain the DLTS results, with temperature scans taken at 2 K intervals within the range 200 K-500 K.

Note 2: The calculation of average visible transmittance

The AVT of a semitransparent device is obtained by weighting the device transmittance spectrum with the AM1.5G photon-flux and the visual response. It can be expressed as:

$$AVT = \frac{\int\limits_{\lambda_{vls}} T(\lambda)V(\lambda)\Phi_{AM1.5G}(\lambda)d\lambda}{\int\limits_{\lambda_{vls}} V(\lambda)\Phi_{AM1.5G}(\lambda)d\lambda}$$

Here $T(\lambda)$ is the total transmittance of the complete device stack, $V(\lambda)$ is the CIE photopic luminosity function, $\Phi_{AM1.5G}(\lambda)$ is the AM1.5G photon flux when this convention is used, and the integration is carried out over the visible range λ_{vis} (typically 380-780 nm). For measured discrete spectra, the integrals are evaluated by summation on a common wavelength grid, and the resulting AVT is reported in percent.

Note 3: **The detailed fitting process of the C-V result**

According to the previous report, the interfacial defect density is related to the difference at zero bias between the defect density measured by C–V (N_{CV}). The depletion region width (W_d) is calculated according to the following expressions:

$$N_{CV} = \frac{-2\varepsilon_{r,n}N_D}{\left(\frac{d\left((1/C^2)\right)}{dV}\right)qA^2\varepsilon_0\varepsilon_{r,p}\varepsilon_{r,n}N_D + 2\varepsilon_{r,p}}$$

$$W_d = \frac{\varepsilon_0\varepsilon_{r,p}A}{C_0}$$

where A symbolizes the device area, ε_0 represents the vacuum permittivity, $\varepsilon_{r,n}$ and N_D refer to the relative permittivity and doping density of CdS, respectively. $\varepsilon_{r,p}$ is the relative permittivity of Sb_2Se_3, while C_0 and C_1 are two quadratic fitting parameters derived from the C–V curves.

Note 4: The detail fitting process for the SCLC result

The dark logarithmic *J-V* curves of both devices are composed of three regions related to the exponent n: the Ohmic region (n=1) at low voltages; as the voltage increases, defects within the device are completely filled by carriers, entering a region of sharply rising current known as the trap-filled limit (TFL), where n>3, and the trap-free child region at high voltages where n=2. The defect density can be calculated using the following formula:

$$N_{trap} = \frac{2\varepsilon_0\varepsilon_r V_{TFL}}{qL^2}$$

In this case, ε_0 represents the vacuum permittivity, ε_r stands for the relative permittivity, VTFL is the starting voltage of the TFL region, q denotes the elementary charge, and L is the thickness of the Sb_2Se_3 layer.

Additionally, for n=2, the trap-free child region can be calculated using the Mott-Gurney law for carrier mobility:

$$J = \frac{9\varepsilon_0\varepsilon_r\mu V^2}{8L^3}$$

In the formula, V represents the applied voltage, and μ represents the charge carrier mobility. By plugging the data into the formula, the charge carrier mobility of both films can be obtained.

Note 5: **The detail fitting process of decay curves based on the TPC and TAS result**

The decay curves of transient photovoltage (TPV), transient absorption spectra (TAS), and transient photocurrent (TPC) were fitted using a biexponential equation:

$$y = A_1 e^{-\frac{x}{\tau_1}} + A_2 e^{-\frac{x}{\tau_2}}$$

The average lifetime τ_{ave} was estimated from the fitting parameters according to equation:

$$\tau = \frac{A_1 \tau_1^2 + A_2 \tau_2^2}{A_1 \tau_1 + A_2 \tau_2}$$

where τ_1 and τ_2 are related to the interface/surface recombination and the bulk recombination, respectively, and A_1 and A_2 are weighting factors correspond to τ_1 and τ_2, respectively.

Note 6: The detailed fitting process of DLTS results

According to the previous report, the defect activation energy (E_a) and carrier trapping cross-section (σ) are key parameters for characterizing deep-level defects in semiconductor materials. These values can be determined from the Arrhenius plot obtained via DLTS measurements. The carrier emission rate (e(T)) is expressed as:

$$e(T) = \gamma\sigma v_{th} N_C exp\left(-\frac{E_a}{kT}\right)$$

Here, γ is a constant related to the effective mass of electrons, σ is the trapping cross-section, v_{th} is the thermal velocity, N_C is the effective density of states in the conduction band, E_a is the activation energy, k is the Boltzmann constant, and T is the temperature.

The linearized form of this equation is:

$$ln\left[\frac{e(T)}{T^2}\right] = ln(\gamma\sigma) - \frac{Ea}{kT}$$

From the slope and intercept of the Arrhenius plot, Ea and σ can be calculated.

The defect concentration (N_t) is related to the capacitance change (ΔC) as:

$$N_t = 2\frac{\lceil \Delta C \lceil}{C_0}N_D$$

$$\tau_{trap} = \frac{1}{\sigma v_{th} N_t}$$

where C_0 is the steady-state capacitance, and N_D is the shallow doping concentration.

Figure S1. Photographic comparison of CdS thin films: the left shows the CdS film deposited from a bath W/O KOH, and the right shows the CdS film deposited from a bath W KOH.

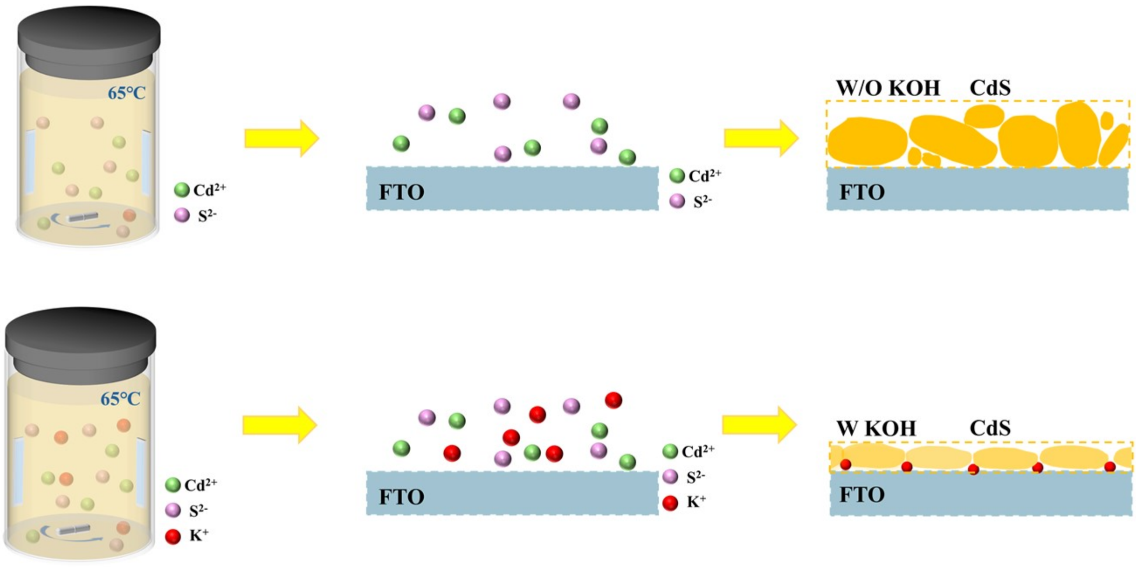

Figure. S2. Schematic illustration of CdS chemical-bath deposition with and without KOH.

During the growth of CdS thin films, simply thinning the layer under conventional conditions often leads to deteriorated crystallinity and roughened surface morphology. In light of extensive previous studies on semiconductor thin-film systems such as CZTS and CIGS, it has been shown that alkali-metal ions are commonly used to regulate the crystallization behaviour of the films. Therefore, in the CdS thinning process, we introduce KOH to achieve simultaneous thinning and crystallization control of the CdS layer. We consider that the primary role of KOH is to modify the pH of the chemical bath, thereby tuning the distribution and reactivity of precursor components in the solution and, in turn, affecting the nucleation and grain-growth kinetics of CdS; on this basis, owing to the relatively large ionic radius of K^+, its adsorption on the crystal surface or partial incorporation into the CdS lattice during deposition can further regulate crystal growth by subtly adjusting the local stress field and structural environment, thereby promoting the formation of CdS films that are thinner yet exhibit higher crystallinity with more compact and uniformly distributed grains.

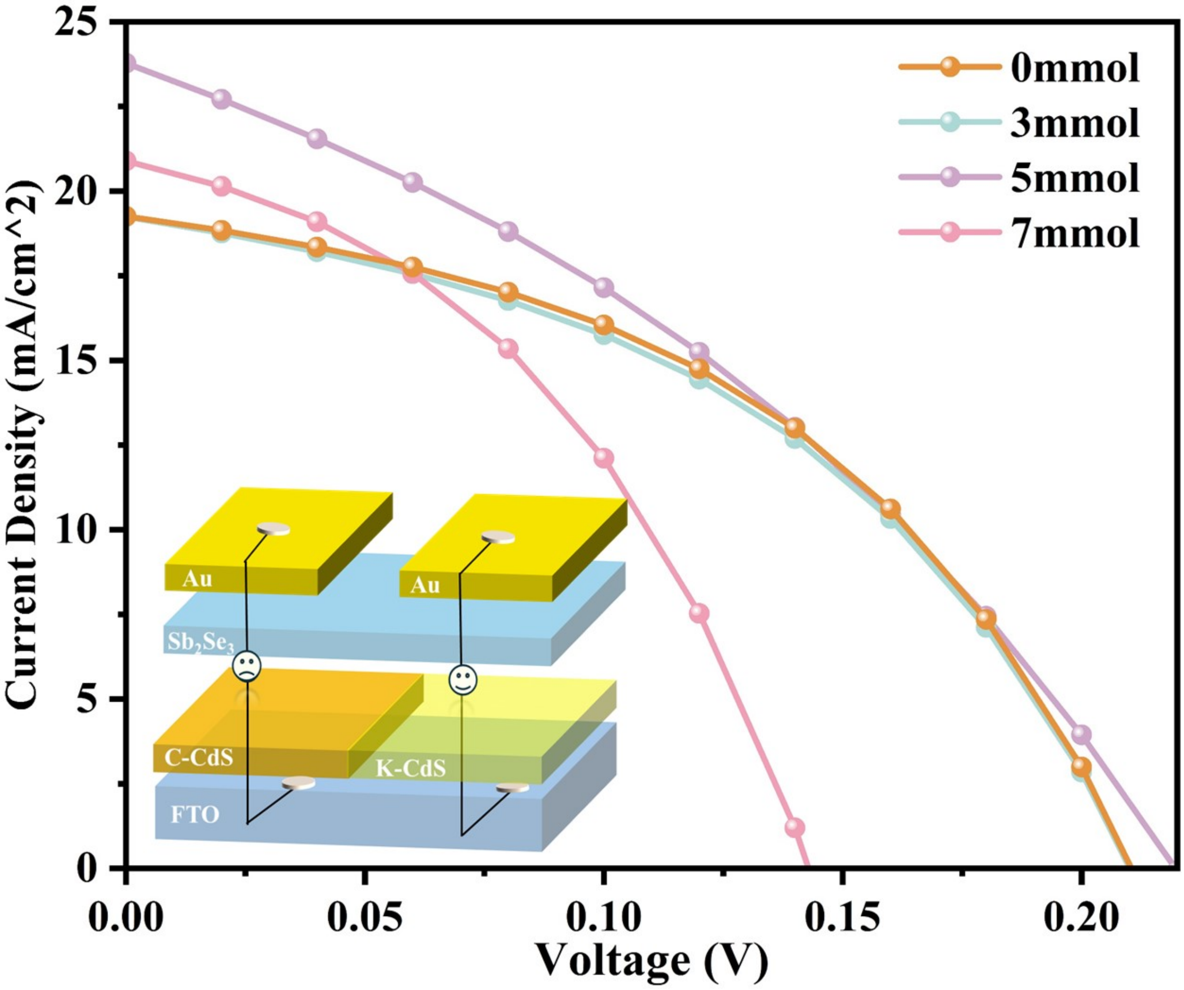

Figure S3. The *J-V* result of Sb_2Se_3 thin film solar cells with various doping amounts of KOH.

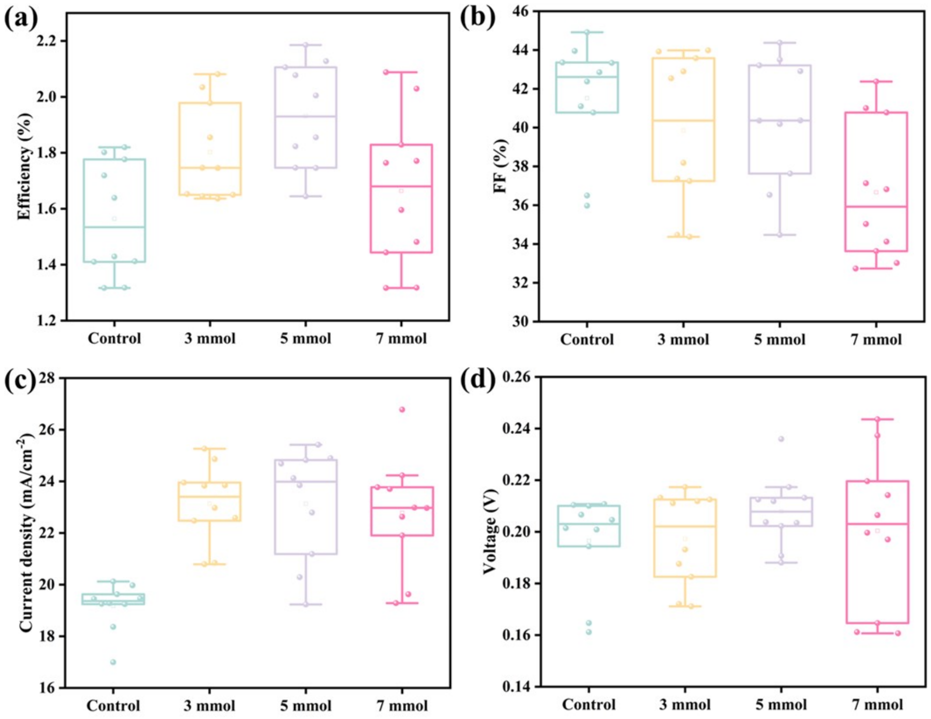

Figure S4. The effects of varying KOH doping amounts on Sb_2Se_3 thin film solar cells were statistically assessed using box plots, focusing on the parameters of (a) *PCE*, (b) FF, (c) J_{SC}, and (d) V_{OC}.

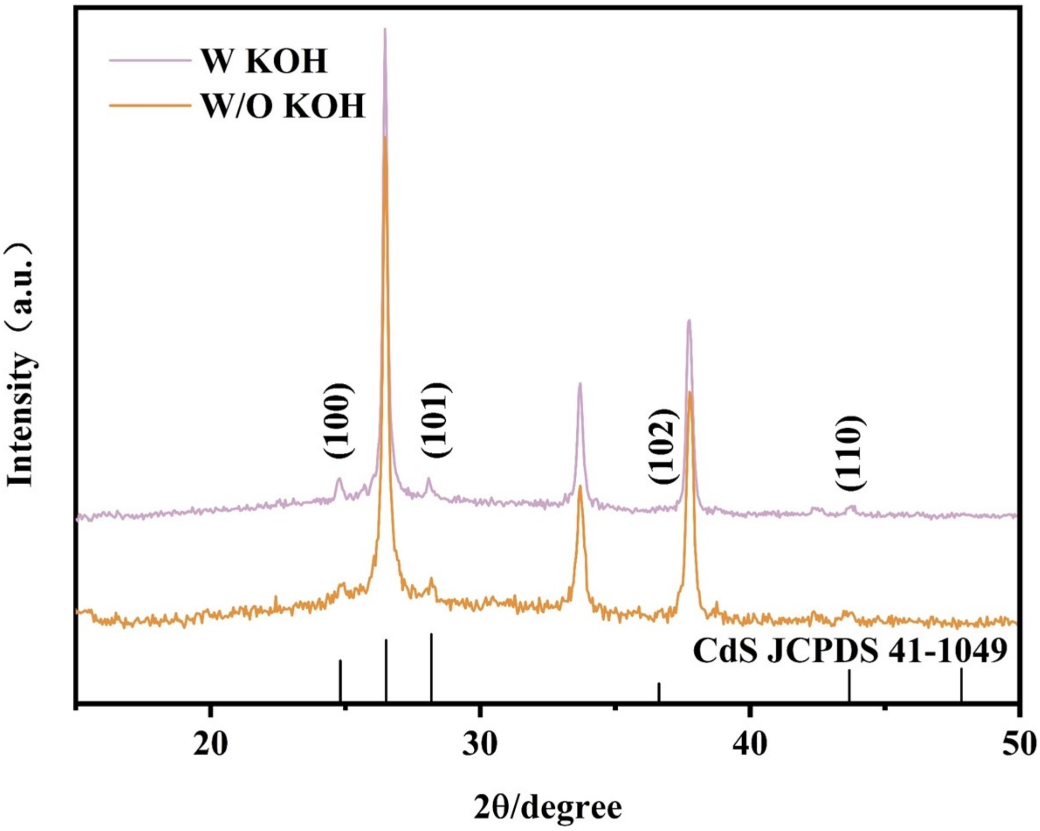

Figure S5. Normalized XRD localized patterns of CdS films deposited from baths W/O KOH and W KOH.

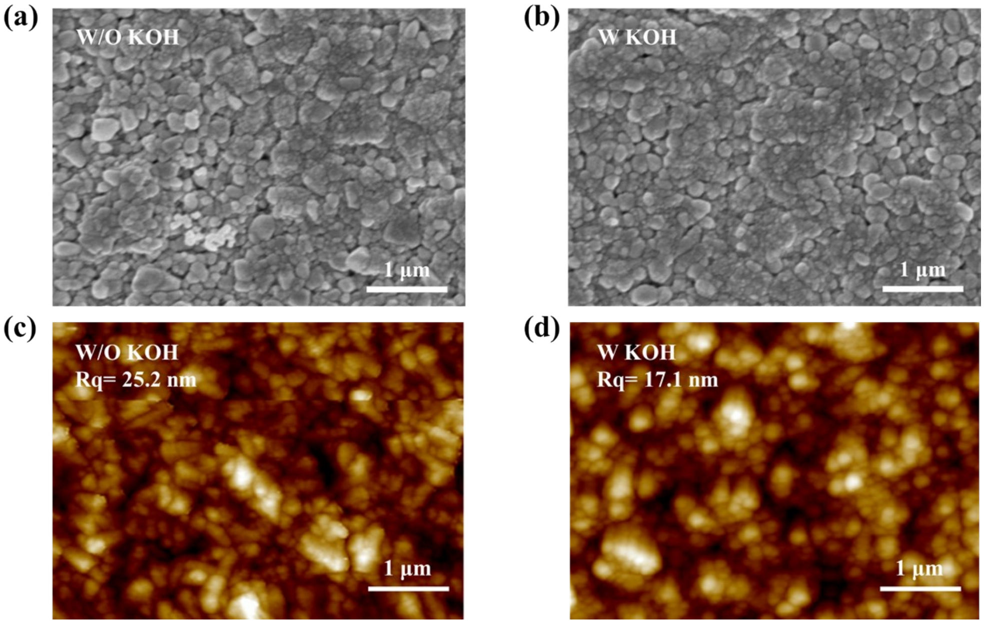

Figure S6. SEM and AFM images of CdS films deposited W/O KOH and W KOH.

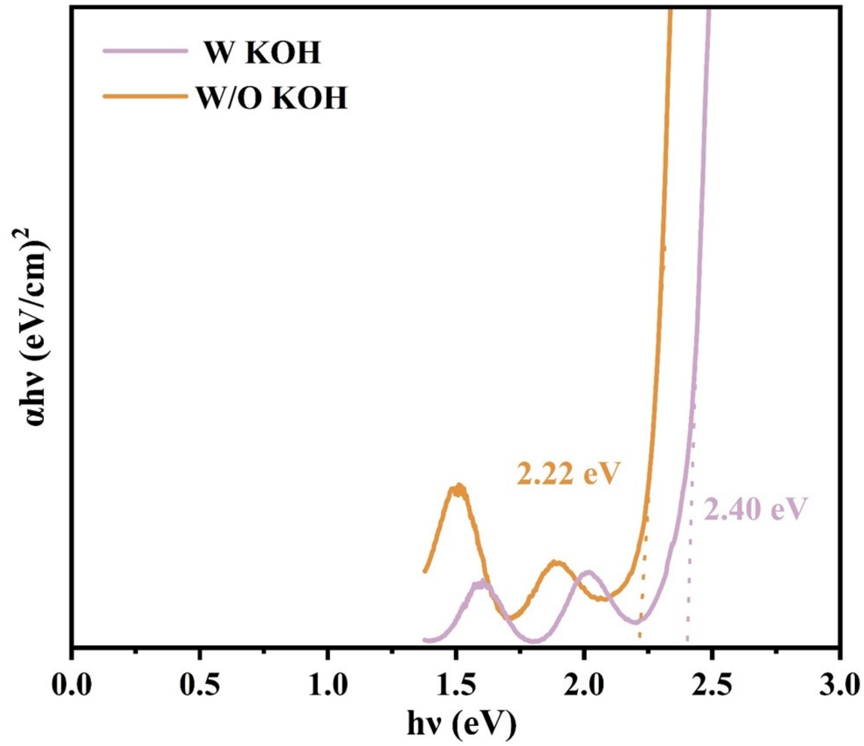

Figure S7. The bandgap result of CdS film with and without KOH.

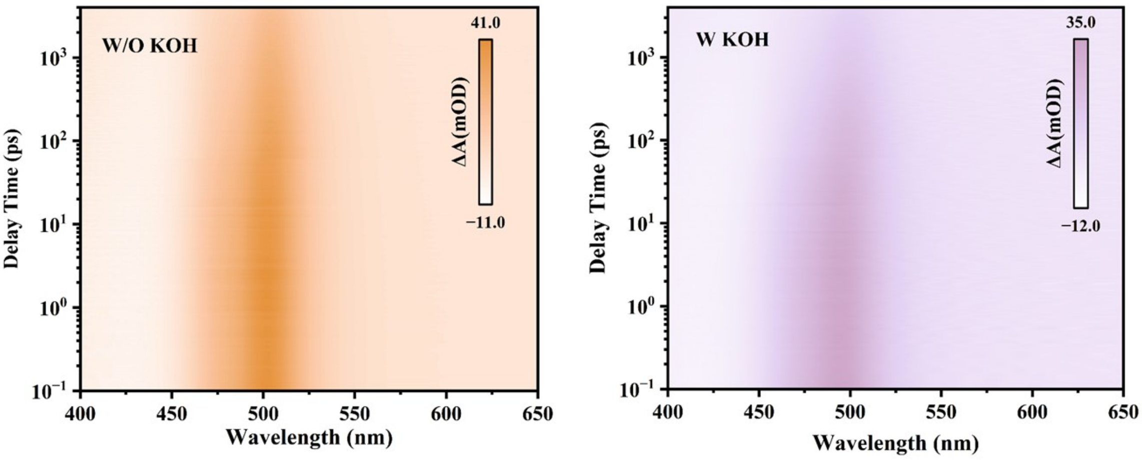

Figure S8. The TAS mapping result of CdS films with and without KOH.

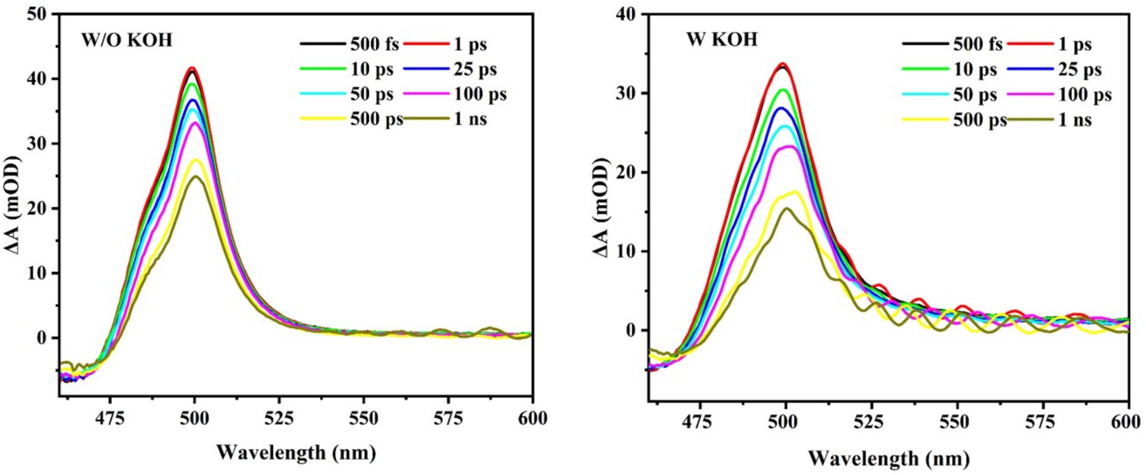

Figure S9. Delay time-dependent TA spectra.

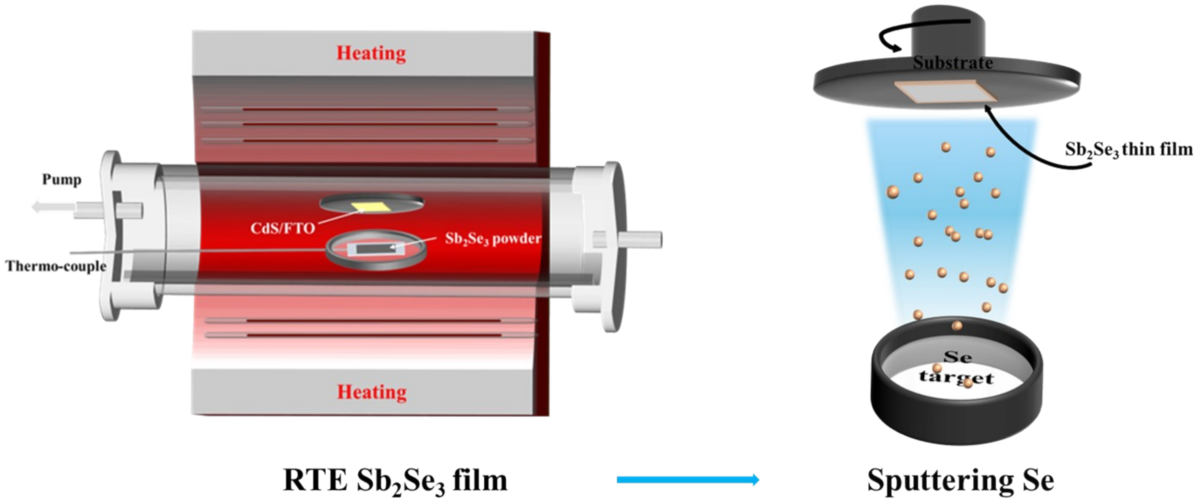

Figure S10. Schematic illustration of the fabrication process for ultrathin semitransparent Sb_2Se_3 films.

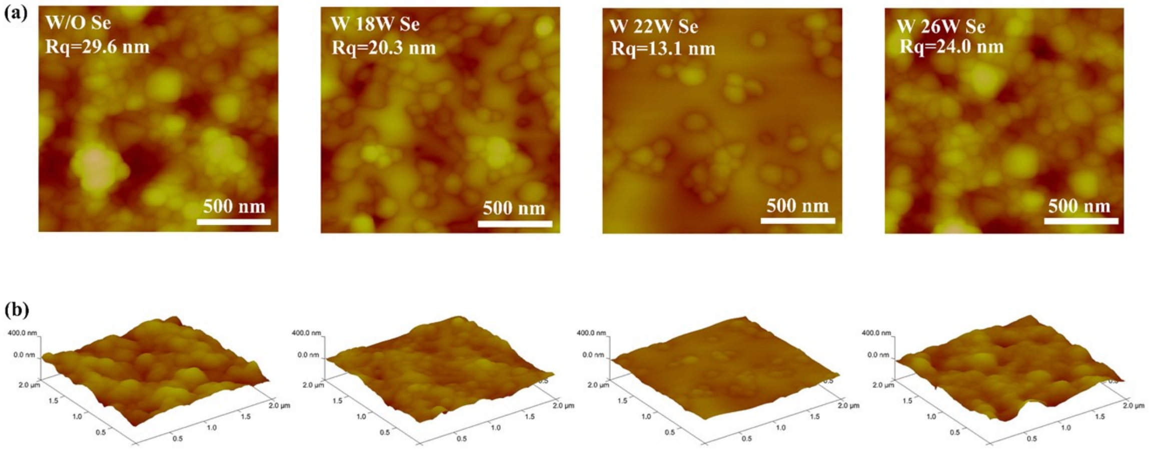

Figure S11. AFM characterization of Se deposition layers under different sputtering powers. (a) 2D surface morphology images and corresponding surface roughness, (b) corresponding 3D surface morphology images.

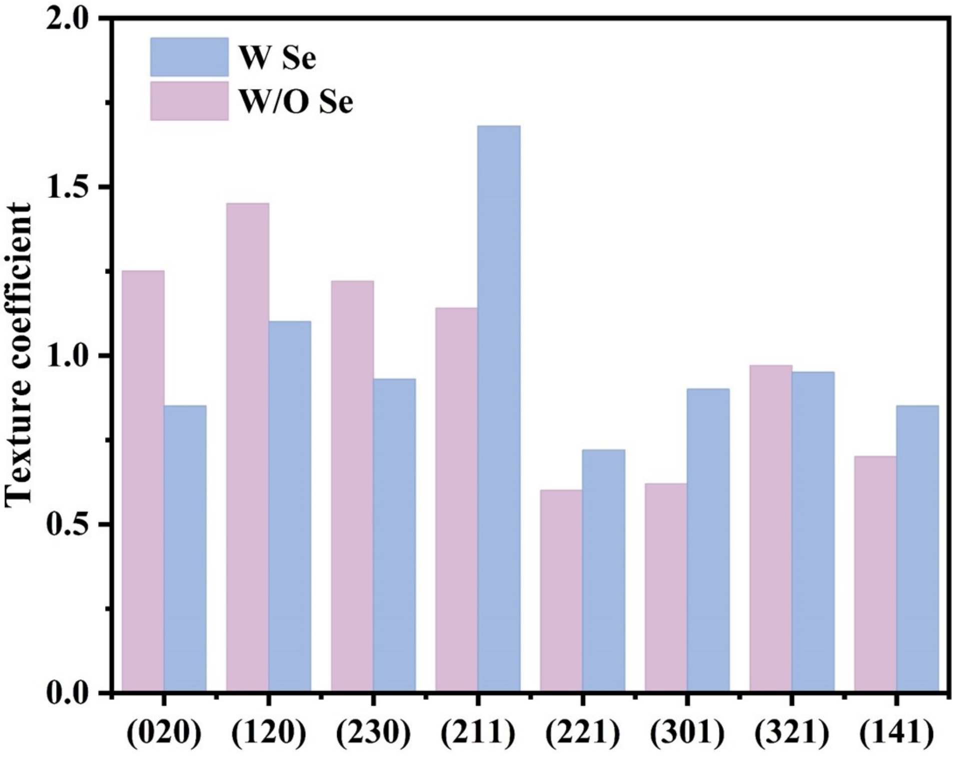

Figure S12. The corresponding TC of Sb_2Se_3 films with and without Se.

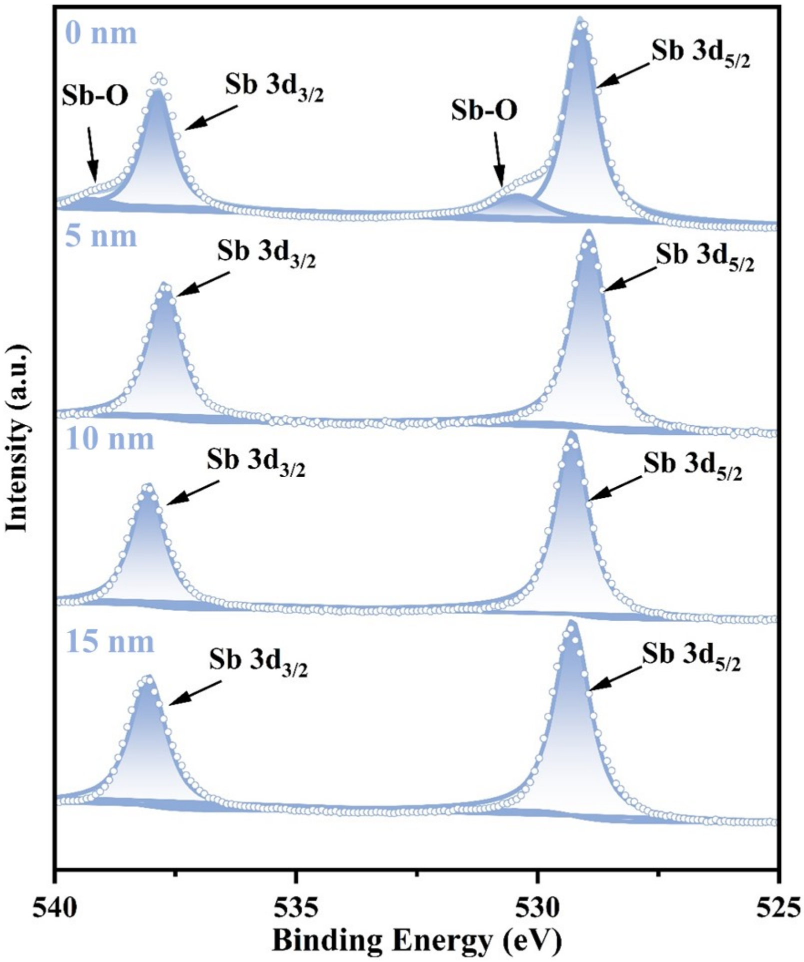

Figure S13. The XPS results from Sb_2Se_3 film with various etching depths from 0-15nm.

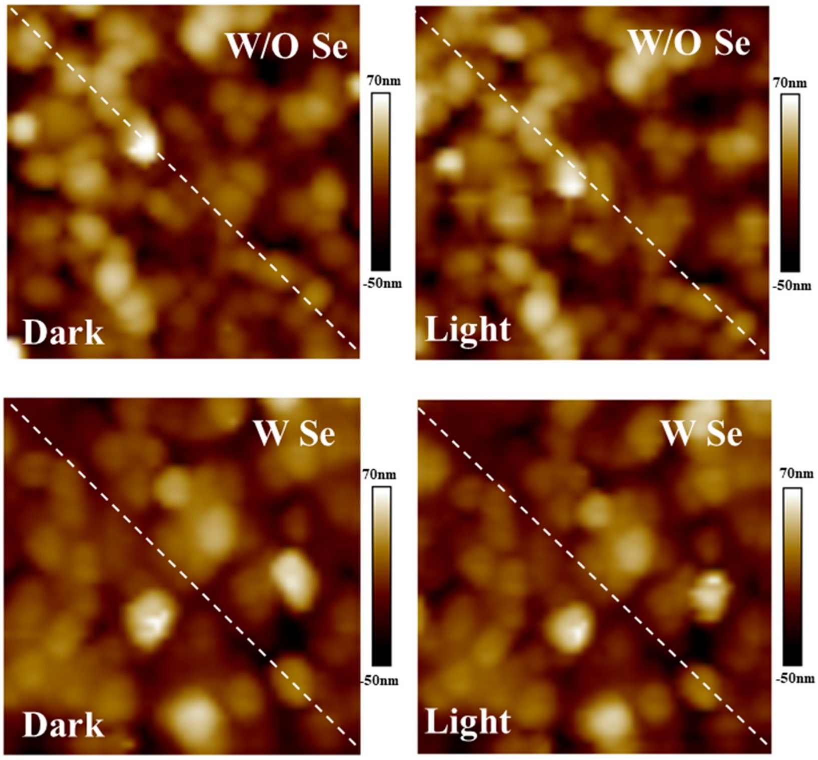

Figure S14. Surface morphology KPFM images of W/O Se and W Se samples.

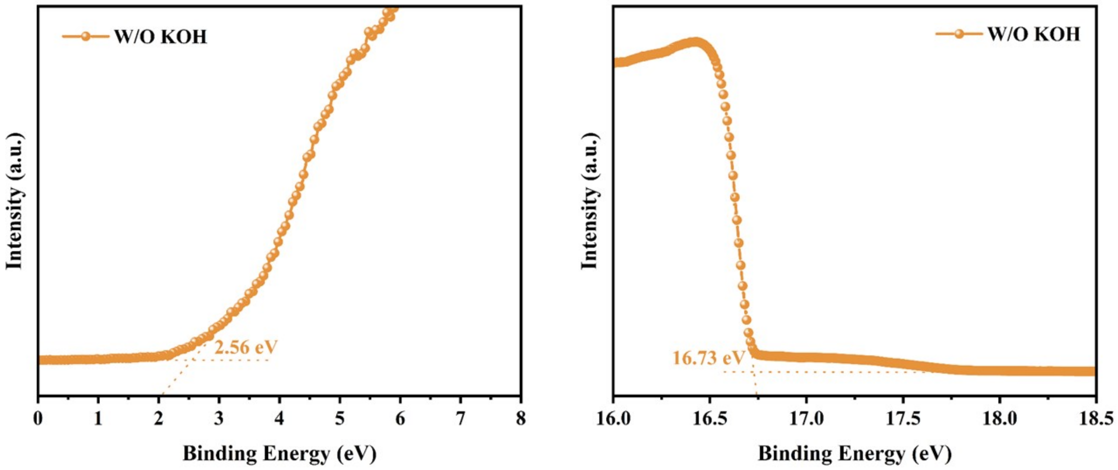

Figure S15. The UPS spectra of the work function edge and the valence-band edge of CdS films without KOH.

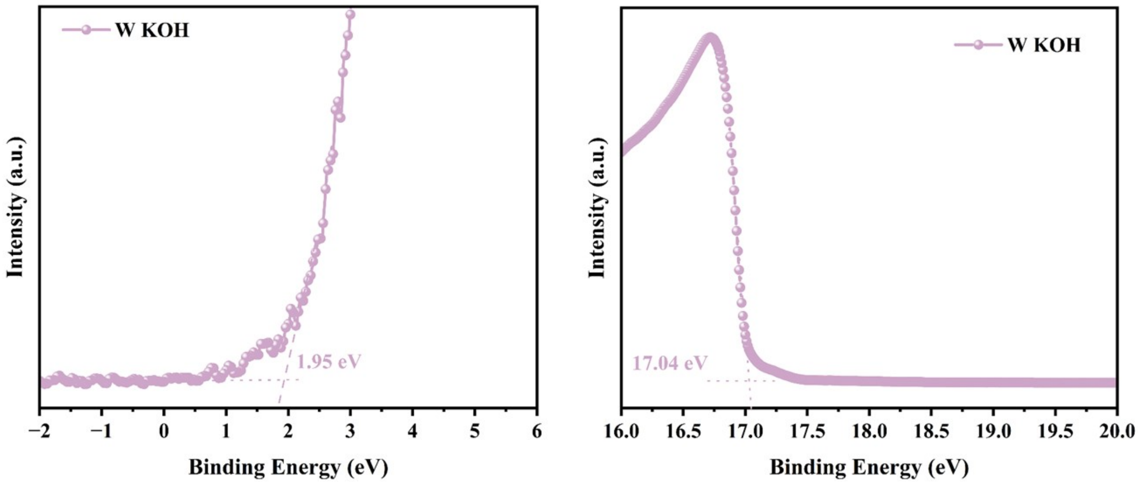

Figure S16. The UPS spectra of the work function edge and the valence-band edge of CdS films with KOH.

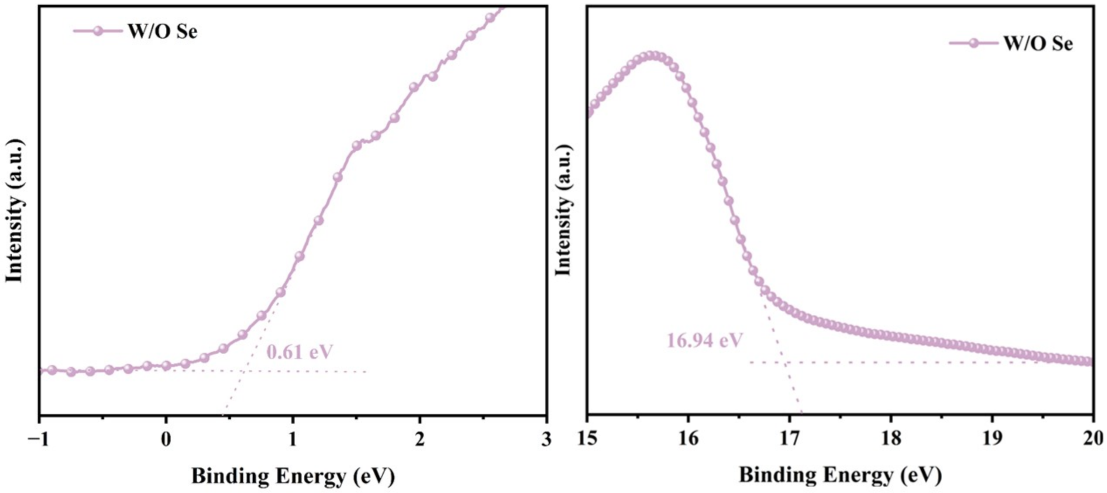

Figure S17. The UPS spectra of the work function edge and the valence-band edge of Sb_2Se_3 films without Se.

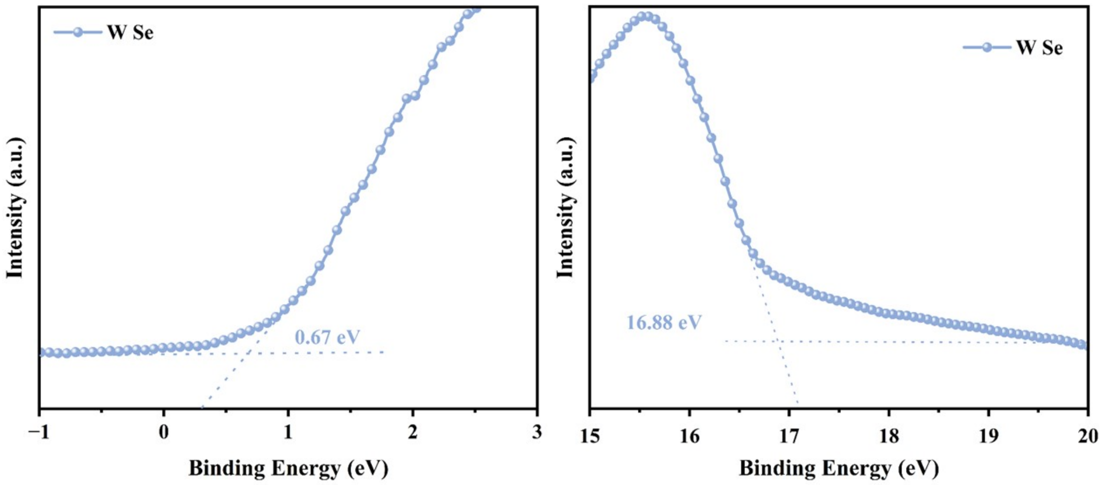

Figure S18. The UPS spectra of the work function edge and the valence-band edge of Sb_2Se_3 films with Se.

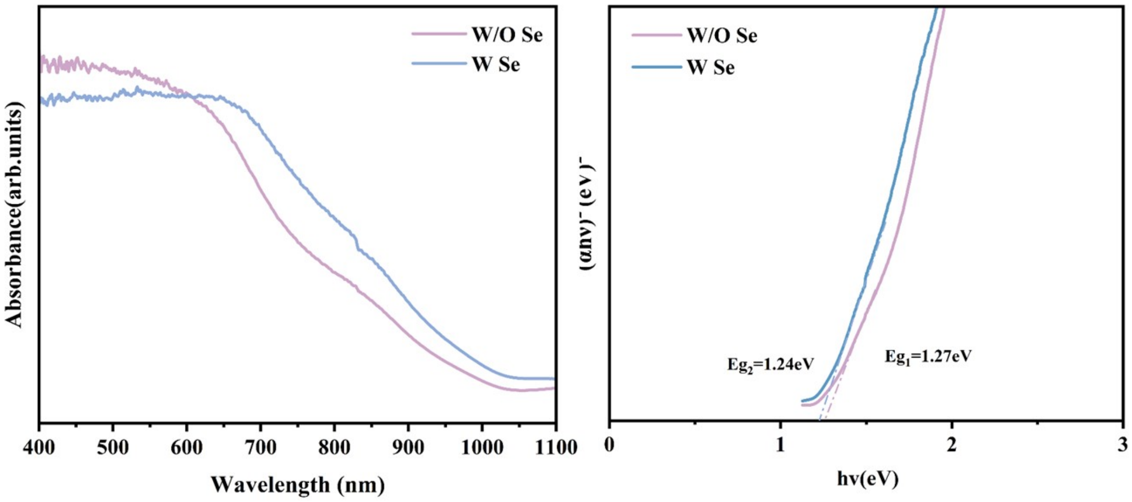

Figure S19. The absorption and bandgap result of Sb_2Se_3 film with and without Se.

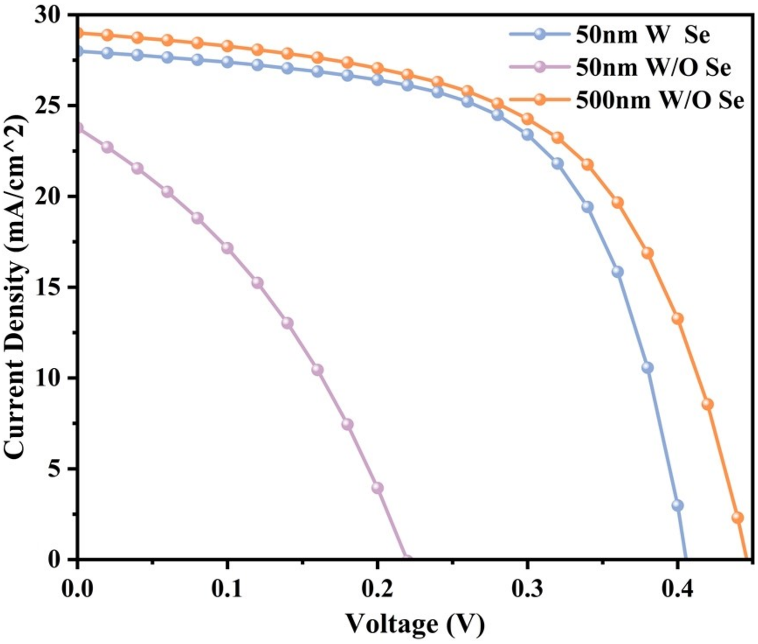

Figure S20. *J-V* curves of Sb_2Se_3 solar cells with different absorber thicknesses and Se-treatment conditions.

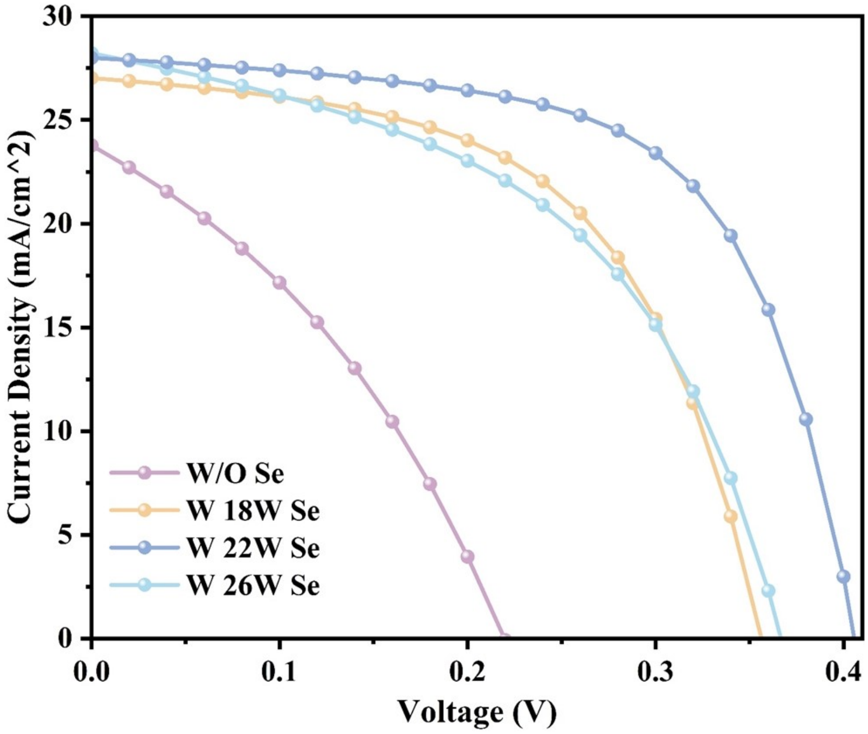

Figure S21. *J-V* characteristics of Sb_2Se_3 solar cells with Se interface layers deposited at different sputtering powers.

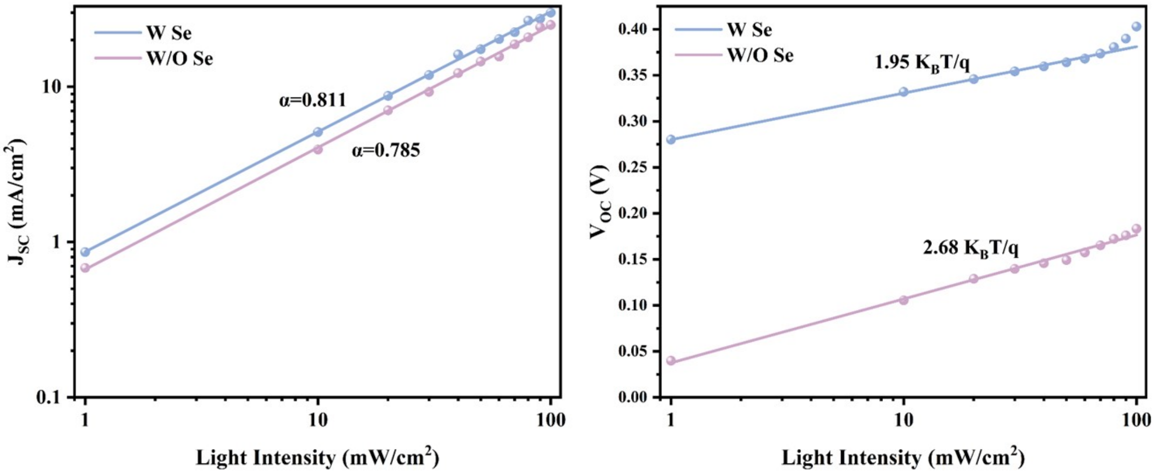

Figure S22. (a)light intensity dependence of J_{SC}, (b) light intensity dependence of V_{OC}.

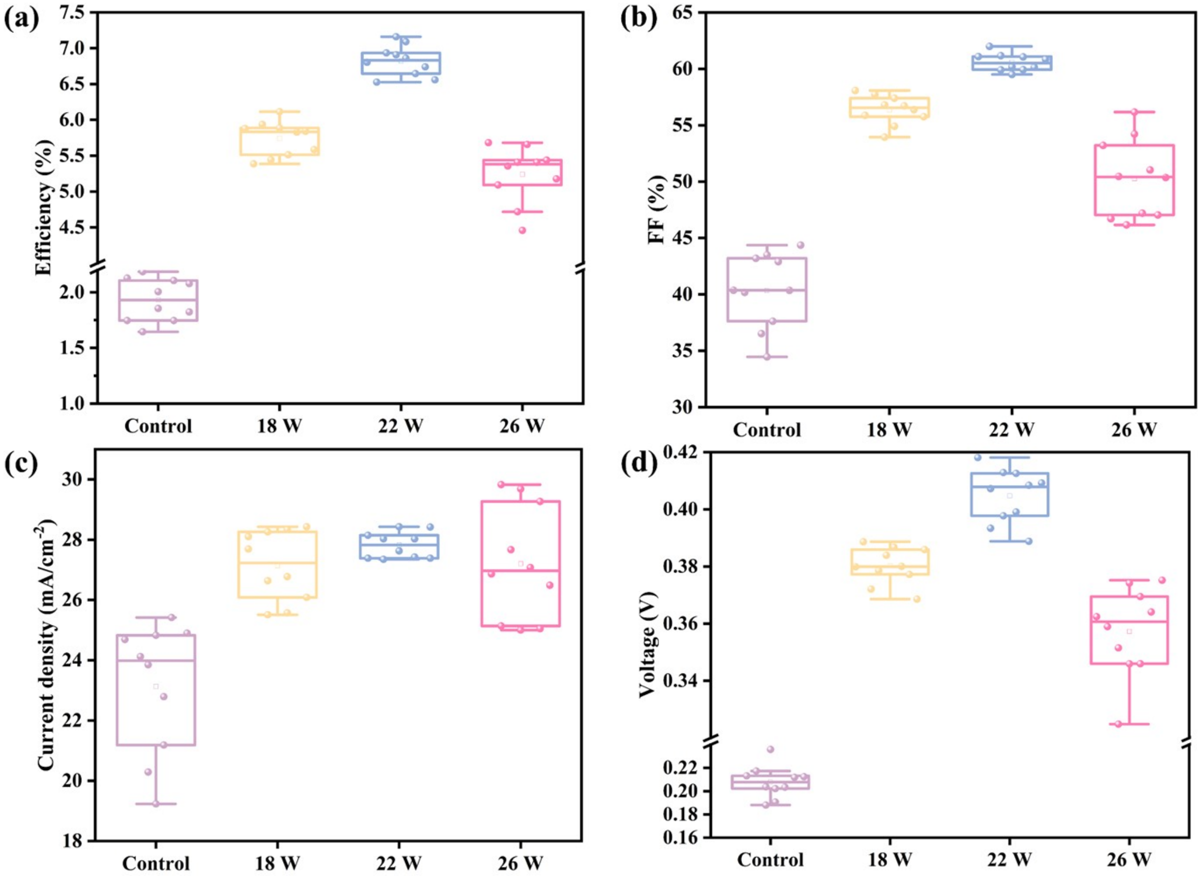

Figure S23. The effects of varying sputtering powers of the Se interface layer on Sb_2Se_3 thin-film solar cells were statistically assessed using box plots, focusing on the parameters of (a) *PCE*, (b) *FF*, (c) J_{SC}, and (d) V_{OC}.

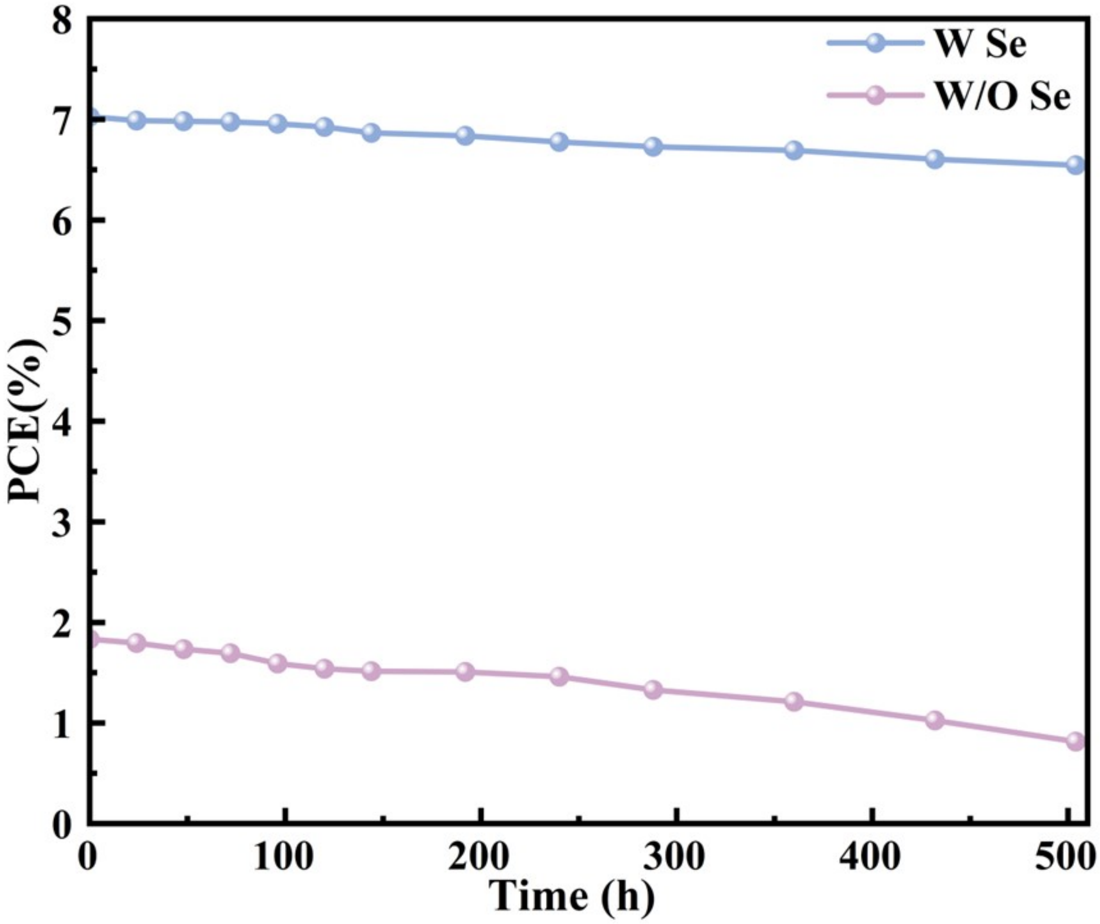

Figure S24. Stability test of W Se and W/O Se Sb_2Se_3 solar cells in ambient air.

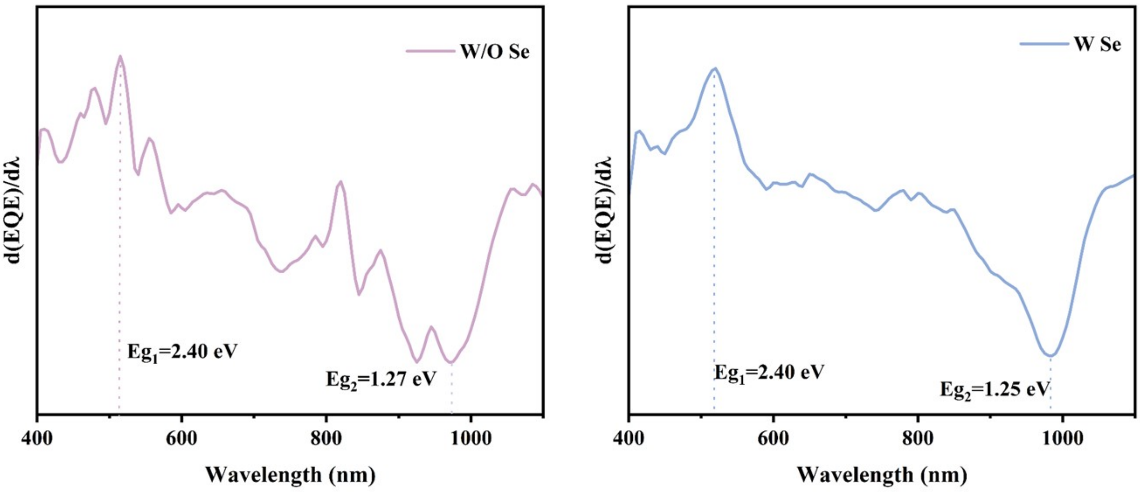

Figure S25. Bandgap analysis based on *EQE* results.

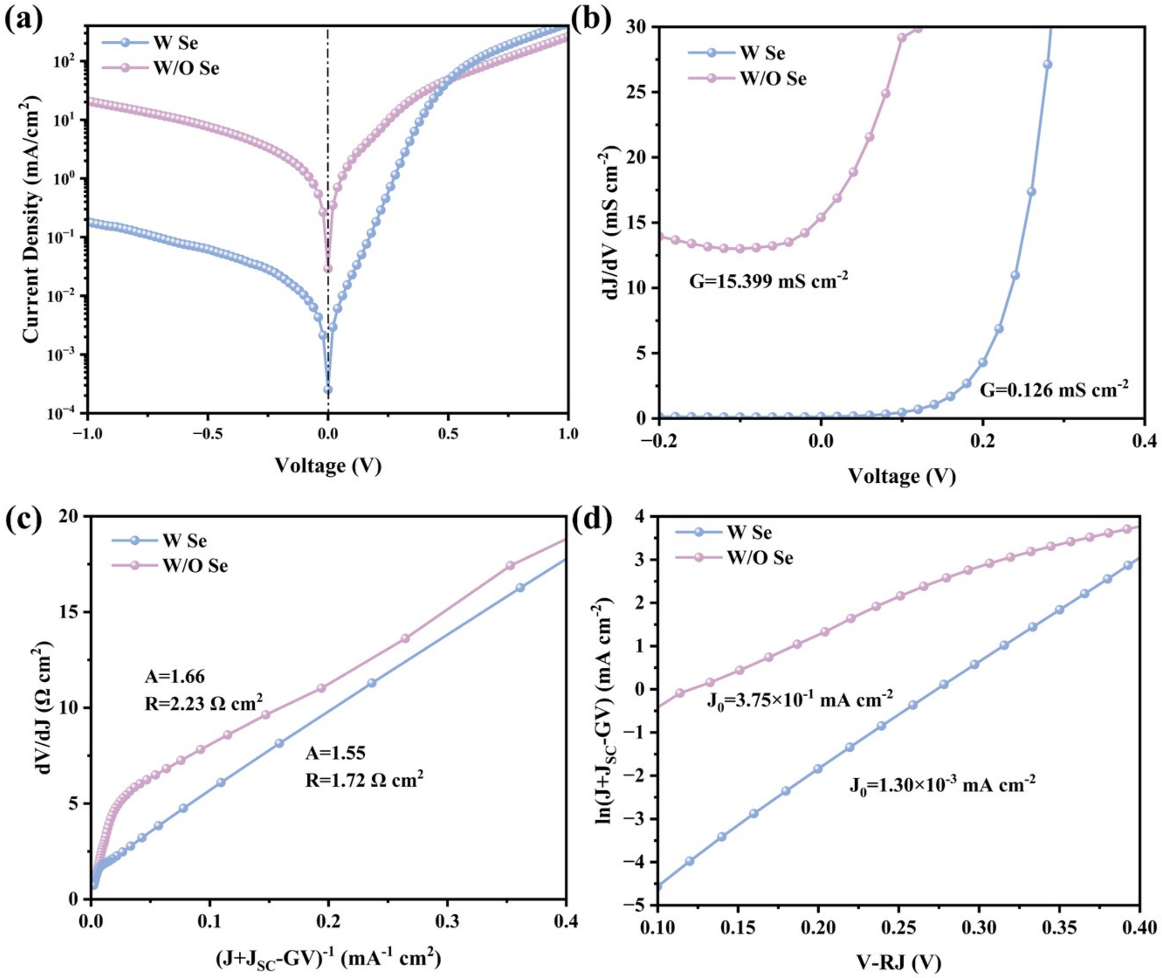

Figure S26. (a) dark J-V plot. (b) dJ/dV vs. V graph for G extraction, (c) dV/dJ vs. $(J+J_{SC}\text{-}GV)^{-1}$ graph for R and A extraction, (d) $\ln(J+J_{SC}\text{-}GV)$ vs. V-RJ graph for J_0 extraction.

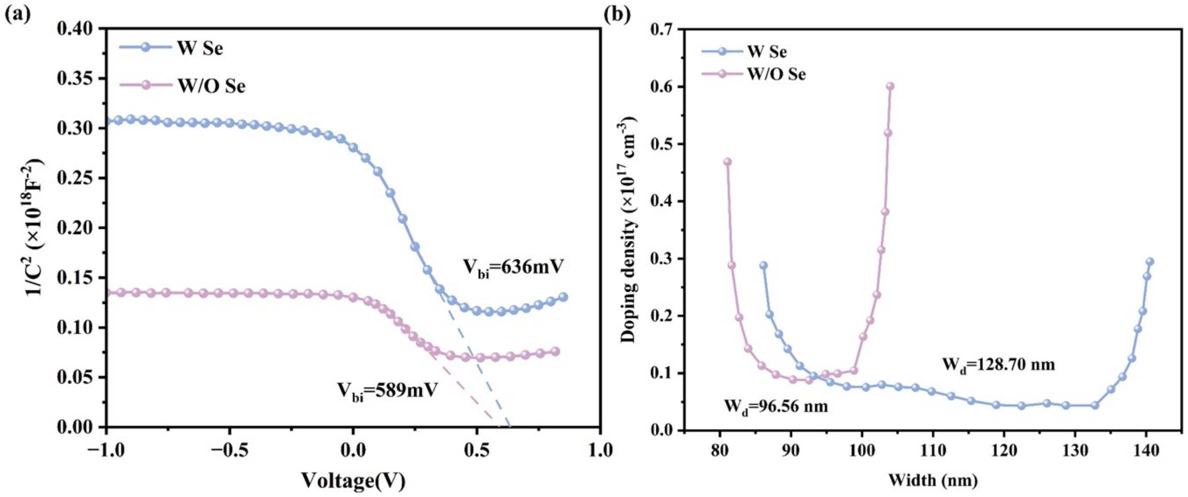

Figure S27. (a)*C-V* curves, (b)N$_{C\text{-}V}$ curves of the W Se and W/O Se devices.

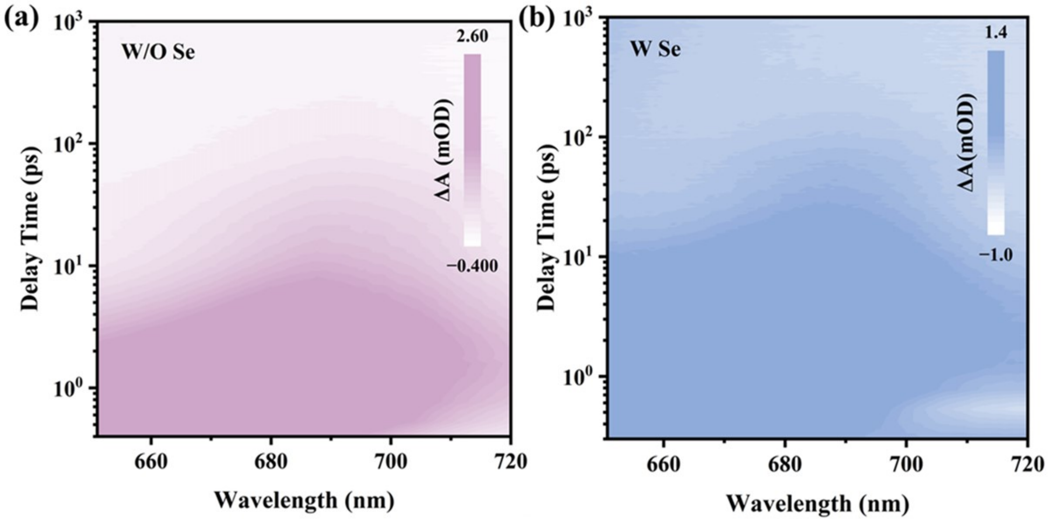

Figure S28. The TAS mapping result of Sb_2Se_3 films with and without Se.